


# Melting relations in the system $\text{FeCO}_3$ – $\text{MgCO}_3$ and thermodynamic modelling of Fe–Mg carbonate melts

Nathan Kang<sup>1</sup>  · Max W. Schmidt<sup>1</sup> · Stefano Poli<sup>2</sup> · James A. D. Connolly<sup>1</sup> · Ettore Franzolin<sup>1</sup>

Received: 1 August 2015 / Accepted: 29 July 2016  
© Springer-Verlag Berlin Heidelberg 2016

**Abstract** To constrain the thermodynamics and melting relations of the siderite–magnesite ( $\text{FeCO}_3$ – $\text{MgCO}_3$ ) system, 27 piston cylinder experiments were conducted at 3.5 GPa and 1170–1575 °C. Fe-rich compositions were also investigated with 13 multi-anvil experiments at 10, 13.6 and 20 GPa, 1500–1890 °C. At 3.5 GPa, the solid solution siderite–magnesite coexists with melt over a compositional range of  $X_{\text{Mg}}$  ( $=\text{Mg}/(\text{Mg} + \text{Fe}_{\text{tot}})$ ) = 0.38–1.0, while at  $\geq 10$  GPa solid solution appears to be complete. At 3.5 GPa, the system is pseudo-binary because of the limited stability of siderite or liquid  $\text{FeCO}_3$ , Fe-rich carbonates decomposing at subsolidus conditions to magnetite–magnesian ferrite solid solution, graphite and  $\text{CO}_2$ . Similar reactions also occur with liquid  $\text{FeCO}_3$  resulting in melt species with ferric iron components, but the decomposition of the liquid decreases in importance with pressure. At 3.5 GPa, the metastable melting temperature of pure siderite is located at 1264 °C, whereas pure magnesite melts at 1629 °C. The melting loop is non-ideal on the Fe side where the dissociation reaction resulting in  $\text{Fe}^{3+}$  in the melt depresses melting temperatures and causes a minimum.

Over the pressure range of 3.5–20 GPa, this minimum is 20–35 °C lower than the (metastable) siderite melting temperature. By merging all present and previous experimental data, standard state (298.15 K, 1 bar) thermodynamic properties of the magnesite melt ( $\text{MgCO}_3\text{L}$ ) end member are calculated and the properties of  $(\text{Fe},\text{Mg})\text{CO}_3$  melt fit by a regular solution model with an interaction parameter of  $-7600$  J/mol. The solution model reproduces the asymmetric melting loop and predicts the thermal minimum at 1240 °C near the siderite side at  $X_{\text{Mg}} = 0.2$  (3.5 GPa). The solution model is applicable to pressures reaching to the bottom of the upper mantle and allows calculation of phase relations in the  $\text{FeO}$ – $\text{MgO}$ – $\text{O}_2$ – $\text{C}$  system.

**Keywords** Siderite · Magnesite · Experimental petrology · Melting relations · Oxidation · Solution model

## Introduction

The stability of carbonates against decarbonation and melting is of considerable interest for understanding the global carbon cycle (Dasgupta and Hirschmann 2010). Carbon solubilities in mantle silicates are low, typically a few ppm and at most 10–20 ppm (Keppler et al. 2003; Shcheka et al. 2006; Panero and Kabbes 2008). Hence, carbon is likely to be stored in a separate phase either oxidized as carbonate(s), carbonated fluids (as documented, for example, in inclusions in diamonds; Wang et al. 1996; Stachel et al. 2000; Klein-BenDavid et al. 2009) or melts or in reduced phases such as diamonds, carbides or Fe–C alloys (Boulard et al. 2012). Computed phase equilibria on sediment bulk compositions and metabasalts as well as phase equilibria experiments on carbonated sediments, basaltic eclogites and peridotites suggest that Ca–Mg–Fe

Communicated by Chris Ballhaus.

**Electronic supplementary material** The online version of this article (doi:10.1007/s00410-016-1283-3) contains supplementary material, which is available to authorized users.

✉ Nathan Kang  
nathan.kang@erdw.ethz.ch

<sup>1</sup> Department of Earth Sciences, Institute of Geochemistry and Petrology, ETH, Clausiusstrasse 25, 8092 Zurich, Switzerland

<sup>2</sup> Dipartimento di Scienze della Terra, Università degli Studi di Milano, Via Botticelli 23, 20133 Milan, Italy

carbonates remain stable beyond arc depths and enter the deeper parts of the mantle with higher melting temperatures than typical modern subduction geotherms (Wallace and Green 1988; Falloon and Green 1989; Yaxley and Green 1994; Molina and Poli 2000; Kerrick and Connolly 2001a, b; Dasgupta et al. 2004; Yaxley and Brey 2004; Dasgupta and Hirschmann 2006; Poli et al. 2009; Mann and Schmidt 2015). At depth greater than 4–5 GPa, experiments indicate that magnesite ( $\text{MgCO}_3$ ) is the most stable carbonate (Biellmann et al. 1993; Fiquet et al. 2002; Isshiki et al. 2004). In general, carbonates tend to have high  $X_{\text{Mg}}$  values compared to coexisting Fe–Mg silicates; typical compositional ranges for peridotites are  $X_{\text{Mg}}^{\text{magnesite-siderite}}$  of 0.93–0.99 (Brey et al. 2008, 2009; Ghosh et al. 2009), for metabasalts 0.67–0.82 (Dasgupta et al. 2004; Yaxley and Brey 2004; Dasgupta et al. 2005), for metapelites 0.3–0.8 (Thomsen and Schmidt 2008; Grassi and Schmidt 2011) and 0.2–0.9 in carbonatites (Buckley and Woolley 1990). Hence, there is ample reason to investigate the Fe-rich side of the magnesite–siderite binary experimentally and to develop a thermodynamic model for the solid and liquid solutions in this system.

At the extreme Fe-rich end, natural siderite is generally associated with ankerite  $\text{CaFe}(\text{CO}_3)_2$  in sedimentary banded iron formations (BIFs; Klein 2005; Kholodov and Butuzova 2008). Before the rise of oxygen ~2.3 Ga ago, BIFs and anoxic shales were not only platform sediments but also abundant on deep ocean floors (Beukes and Gutzmer 2008), but most of the deep deposits have disappeared from the Earth surface via subduction (Polat et al. 2002; Dobson and Brodholt 2005). High-pressure devolatilization and melting in such Fe-rich systems are poorly understood, and experimental investigation of the  $\text{MgCO}_3$ – $\text{FeCO}_3$  system is required to understand the fate of subducted C-bearing BIFs. Siderite also occurs in hydrothermal veins, in extraterrestrial materials such as on Mars (Morris et al. 2010), in the Martian meteorite ALH84001 (Eiler et al. 2002) and in altered igneous rocks.

The melting reaction of pure siderite becomes stable above 6.8 GPa (Tao et al. 2013; Kang et al. 2015) and the melting of pure magnesite above 2.5 GPa (Irving and Wylie 1975). At lower pressures, magnesite decomposes to  $\text{MgO} + \text{CO}_2$ , while siderite decomposition occurs through a redox reaction to magnetite and graphite. Due to the discordance of the graphite– $\text{CO}_2$  (CCO) oxygen buffer with the common Fe buffers (iron–wustite, wustite–magnetite and magnetite–haematite), wustite +  $\text{CO}_2$  only become stable at temperatures higher than siderite stability (Fig. 1).

Experimental studies on the subsolidus phase relations in the  $\text{MgCO}_3$ – $\text{FeCO}_3$  system at 0.2–0.4 GPa, 350–550 °C (Rosenberg 1967), at 1.5 GPa, 600–800 °C (Goldsmith et al. 1962), and at 3.5 GPa, 900–1100 °C (Franzolin et al. 2011) prove that there is continuous solid solution

between siderite and magnesite. Subsolidus phase relations were then thermodynamically modelled within the ternary Ca–Mg–Fe carbonate system at high pressures (Davidson 1994; Franzolin et al. 2011; Holland and Powell 2011). The binary  $\text{MgCO}_3$ – $\text{FeCO}_3$  has recently been studied at 6 GPa and 900–1700 °C (Shatskiy et al. 2015a), where results suggest minor incongruent melting of Mg–Fe carbonate to form oxide–carbonate liquids coexisting with  $\text{CO}_2$  fluid. Phase equilibria studies in particular on compositions near Fe end members are complicated by the fact that at conditions above the iron–wustite buffer, some of the ferrous iron always oxidizes to ferric iron.

This study defines the melting loop of the  $\text{MgCO}_3$ – $\text{FeCO}_3$  binary at 3.5 GPa, 1170–1575 °C, filling a decisive gap on the melting behaviour of iron-bearing carbonates at mantle conditions. In addition, we present experimental data constraining the Fe-rich side of this binary at 10, 13.6 and 20 GPa. Based on the experimental data, we fit the thermodynamic solution model for Mg–Fe carbonate melts considering the influence of  $f_{\text{O}_2}$  and redox reactions of iron-bearing phases. This melt model provides the first approximation for the prediction of Mg–Fe carbonate melting relations at pressure.

## Experimental and analytical methods

### Starting materials

Starting materials were prepared from natural magnesite with an  $X_{\text{Mg}}$  of 0.989 from Obersdorf (Philipp 1998), synthetic magnesite (99.9 %  $\text{MgCO}_3$  powder from Alfa-Aesar) and synthetic siderite. Starting materials for piston cylinder experiments were mixtures of natural magnesite and synthetic siderite, while synthetic magnesite was used in the multi-anvil experiments. Magnesite was dried at 220 °C for ~16 h and then stored at 110 °C. Siderite was synthesized from iron oxalate, sealed into gold capsules of 5.4 mm outer diameter, at 350 °C and 200 MPa in an externally heated cold seal vessel run for 6 days (French 1971). The synthetic siderite had a grey-white, slightly brownish colour. Each newly synthesized siderite batch was analysed by scanning electron microscope and X-ray diffraction, which did yield pure siderite. Siderite was stored at ambient temperature in an evacuated glass desiccator to slow oxidation, but with time develops a more intensive brown colour due to oxidation. Storing siderite at, for example, 110 °C in a vacuum oven to prevent hydration led to more rapid oxidation. Drying siderite is not suitable as it starts to oxidize at 110 °C; hence, our starting materials may have contained small amounts of moisture. To minimize absorbed  $\text{H}_2\text{O}$  and oxidation, siderite was synthesized repeatedly as required and experiments

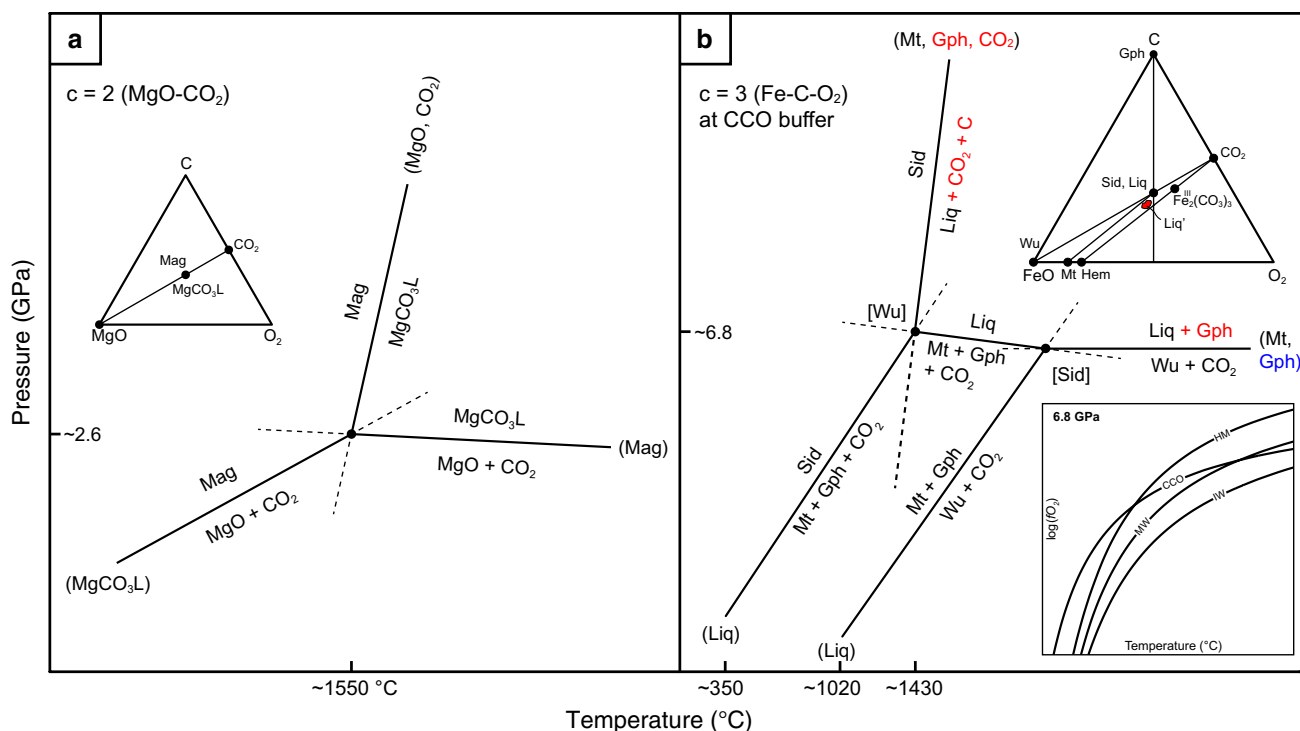


**Fig. 1** Schreinemaker analysis of the melting relations of siderite and magnesite at their lowest melting pressures. The MgO–CO<sub>2</sub> system (**a**) behaves as a true binary and has a simple topology, but phase relations describing siderite melting require three system components (FeO–C–O<sub>2</sub>), opening up a magnetite + graphite field (**b**). Wustite only becomes stable at higher temperatures than siderite stability, a consequence of the discordance between the CCO buffer and the Fe–O buffers (see *insert*). The topology of the FO–C–CO<sub>2</sub> system is drawn for two options: in *black and blue* reactions for a siderite melt with stoichiometric siderite composition, and in *black and red* for siderite melt with a minor ferric component and dissolved CO<sub>2</sub>.

Approximate pressures and/or temperatures are indicated, for magnesite as determined by Irvine and Wyllie (1975) and for siderite as determined by Tao et al. (2013) and Kang et al. (2015). Phase abbreviations in text, figures and tables are: *Wu* wustite; *Carb<sub>ss</sub>* siderite–magnesite solid solution; *Mt<sub>ss</sub>* magnetite–magnesioferrite solid solution; *Gph* graphite; *Liq* carbonate melt (containing Fe oxide quench phases); *Mwu<sub>ss</sub>* wustite–periclase solid solution; *Mag<sub>rem</sub>* magnesite remnant stemming from starting material; *Carb-q* carbonate quench; *Mt-q* magnetite quench; *MgCO<sub>3L</sub>* magnesite liquid; *FeCO<sub>3L</sub>* siderite liquid; *Sid* siderite; *Mag* magnesite; *Mt* magnetite; *Per* periclase

were done in less than 2 months after synthesis. Magnesite and siderite were mixed under alcohol, and after drying, the starting mixtures (Table 1) were stored in a glass dessicator under vacuum.

### Experimental methods

High-pressure experiments were conducted in an end-loaded piston cylinder at 3.5 GPa and in a 1000 ton Walker-type multi-anvil at 10, 13.6 and 20 GPa. Piston cylinder experiments were run with Teflon foil–talc–Pyrex–graphite–MgO assemblies. To avoid Fe loss to metal capsules and prevent the consequent oxidation of the sample, inner graphite capsules were inserted into 3-mm OD Pt capsules, which were welded shut. Run temperatures were controlled by Eurotherm controllers within  $\pm 2$  °C, using B-type (Pt<sub>94</sub>Rh<sub>6</sub>/Pt<sub>70</sub>Rh<sub>30</sub>) thermocouples. The assembly was gradually decompressed after quenching the experiments by turning off the heating power.

Multi-anvil experiments were performed employing tungsten carbide cubes with truncation edge lengths of 11, 8 and 3.5 mm in combination with prefabricated Cr<sub>2</sub>O<sub>3</sub>-doped MgO octahedra of 18, 14 and 10 mm edge length (18/11 assembly for 10 GPa, 14/8 for 13.6 GPa and 10/3.5 for 20 GPa). Assemblies were composed of stepped (18/11, 14/8) or straight (10/3.5) LaCrO<sub>3</sub> heaters, ZrO<sub>2</sub> sleeves, internal MgO spacers and an molybdenum end ring and disc. The starting materials were loaded directly into Au<sub>80</sub>Pd<sub>20</sub> capsules stacked in the central part of the furnace assembly. The 18/11 and 14/8 assemblies contained axial thermocouples, while the 10/3.5 assembly has a thermocouple running across the centre of the furnace (Stewart et al. 2006). Temperature was controlled using a B-type (Pt<sub>94</sub>Rh<sub>6</sub>/Pt<sub>70</sub>Rh<sub>30</sub>) thermocouple for 10 and 13.6 GPa or C type (W<sub>95</sub>Re<sub>5</sub>–W<sub>74</sub>Re<sub>26</sub>) for 20 GPa. Typical thermal gradients across a capsule are 15–25 °C in 18/11 and 14/8 assemblies. Temperature gradients within the 10/3.5 assembly are 30–50 °C over the capsule length of 1.2 mm.

**Table 1** Experimental run conditions and composition (mole fraction) of the run products in the system  $\text{FeCO}_3\text{--MgCO}_3$ 

Sample #	$X_{\text{Mg}}$ Bulk	$P$ (GPa)	$T$ (°C)	Time	Run products Phase assemblage	Carb <sub>ss</sub> $X_{\text{Mg}}$	Liq $X_{\text{Mg}}$	Mt <sub>ss</sub> $X_{\text{Mg}}$	Mwu <sub>ss</sub> $X_{\text{Mg}}$
MS-13	0.1	3.5	1175	5 min	Carb <sub>ss</sub> + Mt <sub>ss</sub>	0.720(94)	–	0.018(6)	–
MS-14	0.1	3.5	1200	5 min	Carb <sub>ss</sub> + Mt <sub>ss</sub>	0.614(43)	–	0.028(4)	–
MS-15	0.1	3.5	1230	5 min	Carb <sub>ss</sub> + Mt <sub>ss</sub>	0.548(26)	–	0.019(4)	–
L-7	0.15	3.5	1170	20 min	Mag <sub>rem</sub> + Mt <sub>ss</sub>	0.984(23) <sup>b</sup>	–	0.118(74)	–
L-8	0.15	3.5	1185	1 h	Mag <sub>rem</sub> + Mt <sub>ss</sub>	0.982(12) <sup>b</sup>	–	0.061(22)	–
L-9	0.15	3.5	1185	25.5 h	Carb <sub>ss</sub> + Mt <sub>ss</sub>	0.847(13)	–	0.071(4)	–
L-10	0.15	3.5	1200	34 h	Carb <sub>ss</sub> + Mt <sub>ss</sub> + Mwu <sub>ss</sub>	0.863(20)	–	0.139(5)	0.343(6)
EF-4	0.20	3.5	1200	22.5 h	Carb <sub>ss</sub> + Mt <sub>ss</sub>	0.377(21)	–	0.000(4)	–
EF-5	0.20	3.5	1250	23 h	Carb <sub>ss</sub> + Liq	0.572(23)	0.310(23)	–	–
EF-6	0.20	3.5	1300	23 h	Liq	–	0.261(27)	–	–
EF-1	0.40	3.5	1200	22.5	Carb <sub>ss</sub> + Mt <sub>ss</sub>	0.448(15)	–	0.001(3)	–
EF-2	0.40	3.5	1250	23 h	Carb <sub>ss</sub> + Liq + Mt <sub>ss</sub> + Mwu <sub>ss</sub>	0.461(72)	0.235(62)	0.011(3)	0.019(3)
EF-3	0.40	3.5	1300	23 h	Carb <sub>ss</sub> + Liq + Mwu <sub>ss</sub>	0.616(32)	0.393(48)	–	0.037(12)
MS-03	0.75	3.5	1200	5 min	Mag <sub>rem</sub> + Mt <sub>ss</sub> + Mwu <sub>ss</sub>	0.968(34) <sup>b</sup>	–	0.241(26)	0.622(41)
MS-02	0.75	3.5	1250	5 min	Carb <sub>ss</sub> + Mt <sub>ss</sub>	0.883(40)	–	0.246(23)	–
MS-04	0.75	3.5	1275	5 min	Carb <sub>ss</sub> + Mwu <sub>ss</sub>	0.916(28)	–	–	0.311(15)
MS-05	0.75	3.5	1300	5 min	Mag <sub>rem</sub> + Mwu <sub>ss</sub>	0.944(56) <sup>b</sup>	–	–	0.744(32)
MS-06	0.75	3.5	1325	5 min	Mag <sub>rem</sub> + Mwu <sub>ss</sub>	0.950(55) <sup>b</sup>	–	–	0.753(15)
MS-07	0.75	3.5	1350	5 min	Carb <sub>ss</sub> + Mt <sub>ss</sub>	0.850(21)	–	0.145(40)	–
MS-08	0.75	3.5	1375	5 min	Carb <sub>ss</sub> + Mt <sub>ss</sub>	0.842(19)	–	0.149(20)	–
MS-09	0.75	3.5	1400	5 min	Carb <sub>ss</sub> + Liq + Mt <sub>ss</sub>	0.846(14)	0.682(115)	0.111(38)	–
MS-10	0.75	3.5	1425	5 min	Carb <sub>ss</sub> + Liq + Mt <sub>ss</sub>	0.880(15)	0.578(195)	0.183(24)	–
MS-11	0.75	3.5	1450	5 min	Carb <sub>ss</sub> + Liq + Mt <sub>ss</sub>	0.881(22)	0.707(171)	0.234(38)	–
MS-12	0.75	3.5	1475	5 min	Carb <sub>ss</sub> + Liq + Mt <sub>ss</sub>	0.865(40)	0.718(50)	0.165(36)	–
MS-16	0.75	3.5	1500	5 min	Carb <sub>ss</sub> + Liq + Mt <sub>ss</sub>	0.877(50)	0.750(46)	0.216(36)	–
MS-17	0.75	3.5	1525	5 min	Liq + Mwu <sub>ss</sub>	–	0.826(26)	–	0.460(12)
MS-18	0.75	3.5	1575	5 min	Liq	–	0.799(28)	–	–
SM-04	0.10	10	1670	20 min	Carb <sub>ss</sub> + Liq	0.145(18)	0.106(18)	–	–
SM-02	0.15	10	1500	20 min	Carb <sub>ss</sub> + Liq	0.217(10)	0.105(70)	–	–
SM-03	0.15	10	1530	20 min	Carb <sub>ss</sub> + Liq	0.229(11)	0.132(41)	–	–
SM-01	0.15	10	1600	20 min	Carb <sub>ss</sub> + Liq	0.204(11)	0.122(25)	–	–
SM-07	0.10	13.6	1700	20 min	Carb <sub>ss</sub> + Liq	0.132(30)	0.095(35)	–	–
SM-05	0.15	13.6	1550	20 min	Carb <sub>ss</sub>	0.200(23)	–	–	–
SM-06	0.15	13.6	1600	20 min	Carb <sub>ss</sub> + Liq	0.175(16)	0.087(29)	–	–
SM20-7	0.10	20	1750	20 min	Carb <sub>ss</sub> + Liq	0.131(33)	0.071(18)	–	–
SM20-9	0.10	20	1840 <sup>a</sup>	5 min	Carb <sub>ss</sub> + Liq	0.248(40)	0.098(70)	–	–
SM20-10	0.10	20	1870	5 min	Carb <sub>ss</sub> + Liq	0.220(39)	0.126(41)	–	–
SM20-1	0.15	20	1550 <sup>a</sup>	20 min	Carb <sub>ss</sub> + Liq	0.225(60)	0.074(80)	–	–
SM20-3	0.15	20	1675	20 min	Carb <sub>ss</sub> + Liq	0.201(48)	0.116(39)	–	–
SM20-2	0.15	20	1725	20 min	Carb <sub>ss</sub> + Liq	0.243(46)	0.123(62)	–	–

Numbers in parentheses are one standard deviation in terms of last digit(s).  $X_{\text{Mg}} = \text{Mg}/(\text{Mg} + \text{Fe}_{\text{tot}})$

<sup>a</sup> Thermocouple breakage during experiment, final temperature estimated

<sup>b</sup> Seed compositions. For abbreviations, see Fig. 1

Quenching was done by turning off the heating power and was followed by pressure unloading for about 15–20 h.

### Analytical techniques

Capsules were mounted longitudinally in epoxy resin and polished to the centre. The open capsules were repeatedly impregnated in low-viscosity resin to avoid mechanical loss of the exposed phases. Experimental charges were analysed with a JEOL JXA8200 electron microprobe (EPMA) to determine phase compositions. Haematite ( $\text{Fe}_2\text{O}_3$ ) and periclase ( $\text{MgO}$ ) have been used as standards for Fe and Mg. The quenched melt was measured at 15 kV acceleration voltage and 6 nA with a beam diameter of 15–20  $\mu\text{m}$  to minimize beam damage. Counting times were 30 s on the peak and 15 s on the background. Note that melt pools with small melt fractions interstitial to grain boundaries were extremely difficult to measure, especially with a defocused electron beam, and contamination by adjacent mineral phases during the measurement could not always be excluded. In such cases, we used an SEM-EDX that allows acquisition using polygonal area measurements.  $\text{CO}_2$  contents of carbonate melts were estimated by difference of the totals to 100. These estimates were within a few per cent of the expected stoichiometric value with respect to  $(\text{Mg,Fe}^{2+})\text{CO}_3$ . Nevertheless, the quenched melt may contain holes or disperse graphite, thus influencing analytical totals. Secondly, the carbonate melts probably contain a small ferric component, and thirdly, they may dissolve molecular  $\text{CO}_2$ , both leading to  $\text{CO}_2$  values different from those of  $(\text{Mg,Fe}^{2+})\text{CO}_3$ . Calculated  $\text{CO}_2$  concentrations were only used to plot liquid compositions in  $\text{FeO-MgO-CO}_2$  projected from graphite.

High-resolution back-scattered electron (BSE) images were obtained from a Jeol JSM 6390LA scanning electron microscope to study textural relationships between phases. Micro-Raman spectroscopy (Horiba Jobin–Yvon LabRam HR 800) was employed to identify the nature of the oxide phases (spinel group vs magnesiowustite). After analysis, all samples were stored in a desiccator.

### Experimental results

Altogether, 40 successful experiments were performed on six different bulk compositions at 3.5, 10, 13.6 and 20 GPa and at temperatures between 1170 and 1890 °C. All experimental run conditions, phase assemblages and their molar compositions are presented in Table 1. Distinctive textural features of the experimental charges at subsolidus and melting conditions at 3.5 GPa and at higher pressure are shown in Figs. 2 and 3.

### Equilibration and run textures

For the supersolidus experiments, 5–20 min run-time was sufficient to attain textural equilibrium. Enhanced by high temperatures and the presence of a liquid phase, equilibrium is evidenced by triple junctions, homogenous phase compositions, completely reacted starting materials and pronounced grain growth of subsolidus carbonates. In general, equilibrium carbonates form discrete large polyhedral grains. The onset of partial melting in experiments is detected using textural criteria. Mostly, the liquid migrates and collects in the hotter zone of the capsule. At low melt fractions, interstitial melt pools along grain edges (Fig. 2d) or concentration of melt along capsule walls are observed (Fig. 2b, c). The carbonate melts are not quenchable, and quench phases from the liquid consist of dendritic aggregates of carbonates (Carb-q, Fig. 2b, c, d, f) intergrown with iron oxides. Where large enough, these quench oxides have been identified by Raman spectroscopy as magnetite (Mt-q), indicating that the melt contains a minor ferric component.

For the subsolidus experiments, textural and compositional equilibrium was more difficult to reach, generally requiring  $\geq 1$ –2 h run-time. Disequilibrium was indicated by irregular grain shapes (Fig. 2a), magnesite-rich mineral cores and compositionally zoned carbonates. The only result that is used from the subsolidus experiments is the carbonate compositions, assuming that the measured carbonate compositions are (meta)stable at run condition.

Bubbles indicating gas or fluid saturation were rarely observed (Figs. 2, 3), also not in the capsules where considerable equilibrium magnetite formed through reaction (1). In the subsolidus runs, this may indicate that the copious amounts of  $\text{CO}_2$  resulting from reaction (1) were contained in the porosity of the graphite capsule; in supersolidus experiments, all of the  $\text{CO}_2$  may be dissolved in the melt. The latter is also indicated by the coexistence of three Fe–Mg phases + graphite, the phase rule only allowing for four phases in this system. Regarding oxygen fugacity, the graphite– $\text{CO}_2$  buffer hence represents only an upper limit, and supersolidus experiments with all  $\text{CO}_2$  dissolved in the melt may have a reduced  $\text{CO}_2$  activity and hence an oxygen fugacity slightly below CCO.

### Auto-redox dissociation, decarbonation and metastable equilibrium

All textural and chemical features of the melting experiments in Pt–C double capsules at 3.5 GPa indicate equilibrium; however, this equilibrium is at least in part metastable. Metastable equilibria can be experimentally investigated at appropriate run durations, profiting of transition phases governed by intermediate steps of minima in the free energy

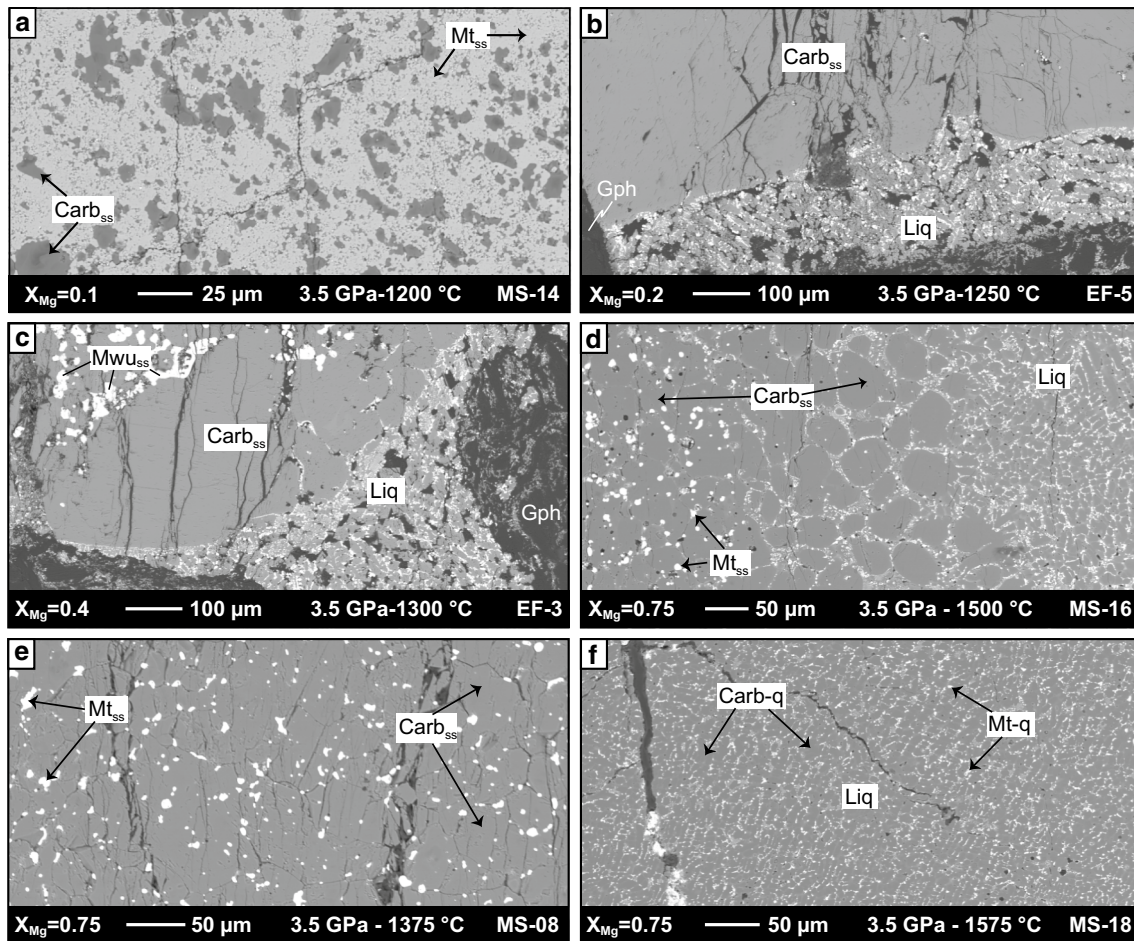
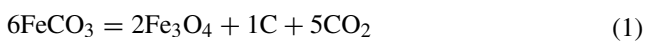


**Fig. 2** Back-scattered electron (BSE) images of typical run products at 3.5 GPa showing subsolidus, near-solidus and supersolidus conditions. **a** Carbonates at subsolidus conditions with substantial decomposition to magnetite solid solution. Note that the bulk  $X_{Mg}$  is 0.1, but the resulting carbonate has  $X_{Mg} = 0.61$ . **b** Partial melting of carbonates to dendritic carbonate melt consisting of carbonate quench and iron oxide fractions. Some melt infiltrates the innermost part of the graphite capsule (*bottom* of image). **c** Stable Fe–Mg carbonates

coexisting with carbonate melt and some wüstite. **d** Carbonate melt coexisting with crystal carbonates; quenched carbonate melts are interstitial to the rounded carbonate grains. **e** At subsolidus conditions, discrete carbonates appear with minor  $Mt_{ss}$  at low run-times. **f** At supersolidus condition, carbonates are completely molten with an intergrowth of carbonate and magnetite quench. For abbreviations, see Fig. 1

surface, according to the Ostwald step rule (see Putnis 1992). Metastable equilibrium melting of mullite has been extensively investigated in the system  $Al_2O_3$ – $SiO_2$  at room pressure (see Pask 1996 for a review) and of muscovite in the system  $K_2O$ – $Al_2O_3$ – $SiO_2$ – $H_2O$  (Brearley and Rubie 1990; Rubie and Brearley 1990) at 0.1 GPa, revealing that metastable liquids can persist over geologic timescales.

The range of compositions on the join magnesite–siderite for which metastable melting occurs cannot be predicted a priori; as a consequence, run durations were optimized following a trial-and-error procedure. Initial run-times were 24 h, but had to be shortened to 5–20 min in order to minimize auto-redox dissociation of the siderite component:



(French 1971; Weidner 1972; Koziol 2004; Tao et al. 2013; Kang et al. 2015). This reaction progresses slowly with time, shifting the composition of the coexisting solid and liquid carbonate phases towards the Mg side. At least part of the resulting ferric iron and probably most of the  $CO_2$  are dissolved in the melt. Our results indicate that supersolidus experiments equilibrate almost instantly (5–20 min), while subsolidus experiments result in polygonal textures with  $120^\circ$  triple junction after 1–2 h. However, run durations of 1–2 h in the supersolidus led to extensive redox dissociation in Fe-rich compositions rendering the choice of the optimal run duration difficult. Experiments directly run in  $Au_{80}Pd_{20}$  capsules resulted in minor  $Fe^0$  loss causing a slightly stronger net oxidation of the charge.

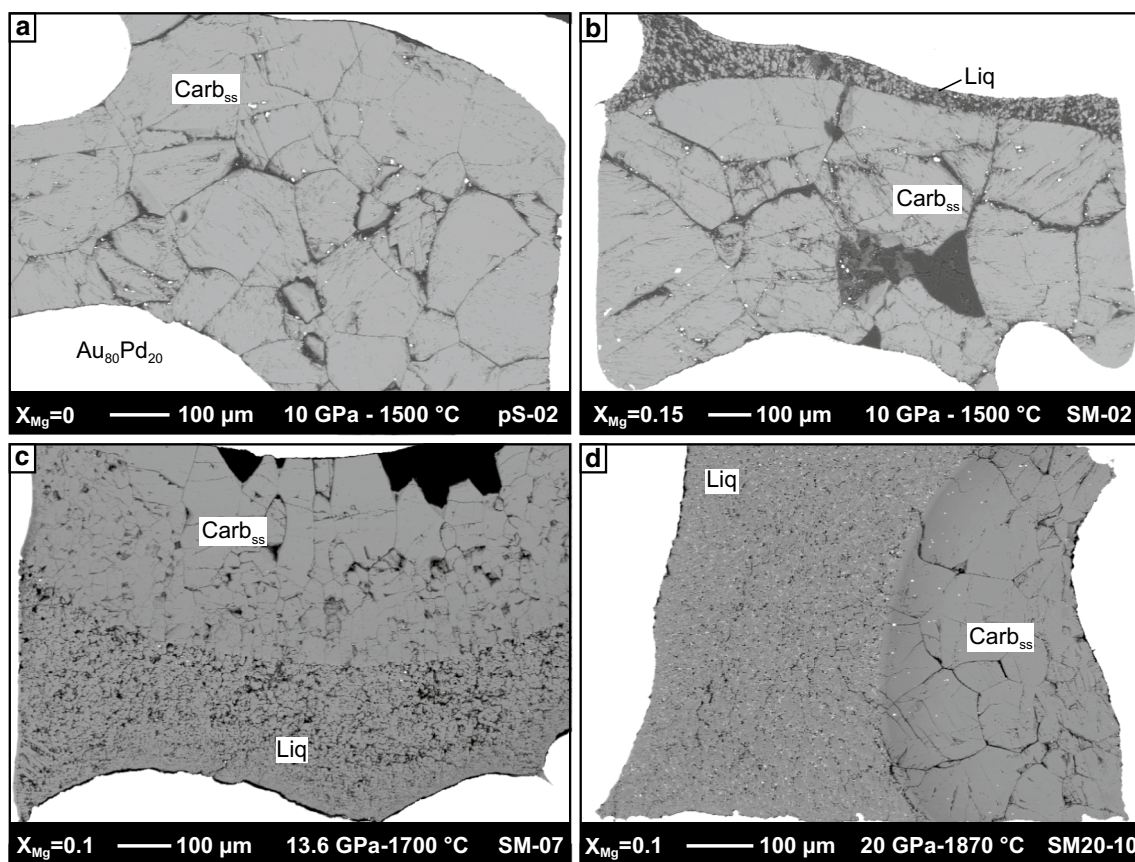
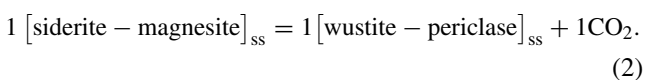


**Fig. 3** BSE images of run products at 10–20 GPa. **a** Monomineralic stable siderite assemblage in gold–palladium capsule at 10 GPa, 1500 °C from Kang et al. (2015). **b** Low degree of partial melting of Mg-bearing siderite with the starting composition  $\text{Mg}_{0.15}\text{Fe}_{0.85}\text{CO}_3$  at 10 GPa, 1500 °C. A similar amount of melt persists over a tem-

perature range of 30–200 °C and is interpreted as melting caused by small amounts of  $\text{H}_2\text{O}$  present in the capsule (see text). **c** Coexistence of siderite–magnesite solid solution with Fe–Mg carbonate melt at 13.6 GPa, 1700 °C. **d** Melting of Fe–Mg carbonates at 20 GPa, 1860 °C. For abbreviations, see Fig. 1

### The siderite–magnesite join at 3.5 GPa

The most critical compositions of run products at 3.5 GPa (Table 1) are depicted in 10 isothermal triangular sections (Fig. 4) saturated in graphite. The compositions of the experimental carbonate liquid and solid pairs are shown in an isobaric  $T$ - $X$  diagram (Fig. 5) of the siderite–magnesite join. Unfortunately, this system is generally characterized by either the auto-redox dissociation (1) of the siderite component or the simple decarbonation reaction of siderite–magnesite solid solution:



The oxide phases are composed of large and idiomorphic grains (up to  $\sim 100 \mu\text{m}$ ), identified as magnetite–magnesioferrite solid solution ( $(\text{Mg}, \text{Fe}^{2+})\text{Fe}_2^{3+}\text{O}_4$ ) or magnesiowustite ( $(\text{Mg}, \text{Fe}^{2+})\text{O}$ ). As argued below, the experiments are most likely not on the CCO ( $\text{C}-\text{CO}-\text{CO}_2$ ) oxygen

fugacity buffer, lending support to the hypothesis that the  $\text{CO}_2$  produced by reactions (1) and (2) may completely dissolve in the melt.

The textures and compositions of the experimental run products were used to define the liquidus and solidus phase boundaries between carbonate liquid (Liq) and solid ( $\text{Carb}_{\text{ss}}$ ). Bulk and phase compositions are expressed on a molar basis, i.e.  $X_{\text{Mg}} = \text{Mg}/(\text{Fe}_{\text{tot}} + \text{Mg})$  (Table 1). Sub-solidus phase assemblages change considerably at different bulk  $X_{\text{Mg}}$ . The amount of magnetite–magnesioferrite solid solution ( $\text{Mt}_{\text{ss}}$ ) in the run products increases with Fe content in the bulk. At temperatures of 1170–1230 °C and bulk  $X_{\text{Mg}}$  of 0.1–0.15, crystal aggregates are dominantly composed of  $\text{Mt}_{\text{ss}}$  and little carbonate (Fig. 2a). Some of the initial experiments (e.g. L-7 and L-8) exhibit large almost unreacted magnesite ( $X_{\text{Mg}}$  of  $\sim 0.94$ – $0.98$ ) grains up to  $\sim 180 \mu\text{m}$ ; in subsequent experiments, care was taken to grind the starting materials to  $< 10 \mu\text{m}$  grain size. Experiments with Pt–C double capsules do not inhibit completely the auto-redox dissociation (1) and decarbonation reaction

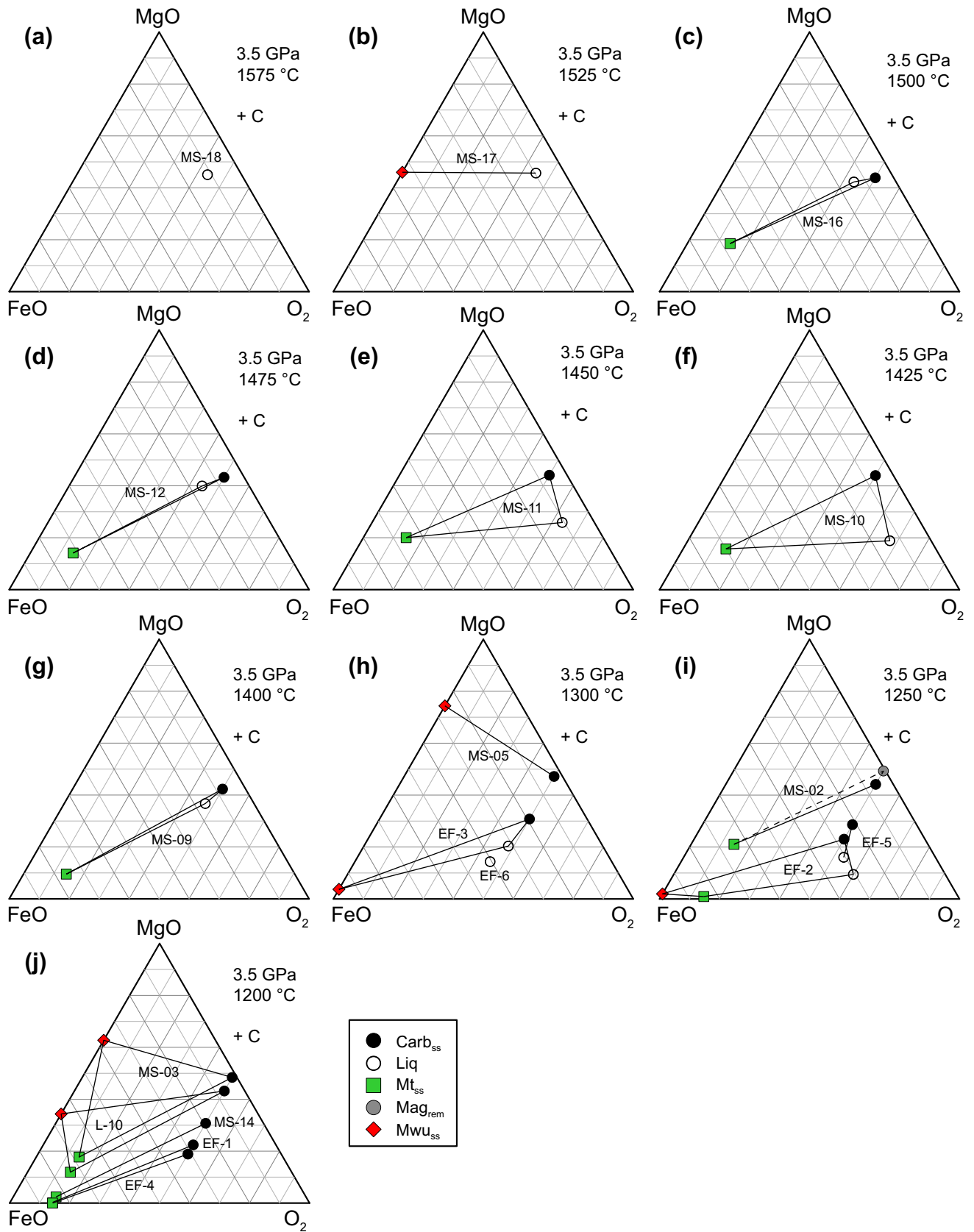




**Fig. 4** Triangular isothermal sections of the most critical experimental runs showing compositions of run products in the FeO–MgO–O<sub>2</sub> system projected through graphite from 1575 to 1200 °C at 3.5 GPa. Note that melt compositions in (e, f) exhibit large standard deviations (see also Fig. 5; Table 1). Coexisting phases within each experiment were connected by *solid tie lines*. *Symbol or tie-line labels* indicate experiment number, see also Table 1. For abbreviations, see Fig. 1

(2) of the siderite component, even with short run-times (5 min, Fig. 2d, e, f). Experimental products at subsolidus conditions with bulk  $X_{\text{Mg}} = 0.2\text{--}0.4$  have Carb<sub>ss</sub> and Mt<sub>ss</sub>. At higher bulk  $X_{\text{Mg}}$ , the run products had magnesio-wüstite (Mwu<sub>ss</sub>) as the dominant oxide phase, its abundance generally increasing with run duration (Fig. 2c) and temperature. Subsolidus phase assemblages with a bulk  $X_{\text{Mg}}$  of 0.75 appear at temperatures up to ~1380 °C. These

experimental charges contain mostly crystal aggregates of (Fe,Mg)CO<sub>3</sub> and very minor oxide phases, either Mt<sub>ss</sub> or Mw<sub>ss</sub> or both.

Solid phase assemblages do not invariably include oxide phases, e.g. where first partial melting of carbonates occurs at 1250 °C with bulk  $X_{\text{Mg}}$  of 0.2, crystals consist essentially of Carb<sub>ss</sub> (Fig. 2b). Carbonate melt is recognized by dendritic intergrowth of carbonate and oxide quench fractions. The measured melt compositions range from  $X_{\text{Mg}} = 0.212$  to 0.826. Experiments with a higher bulk  $X_{\text{Mg}}$  of 0.75 show the onset of partial melting from ~1400 °C upwards, and these experimental charges are characterized by some minor unavoidable Mt<sub>ss</sub> (Fig. 2d). Complete melting is obtained at 1575 °C (Fig. 2f).

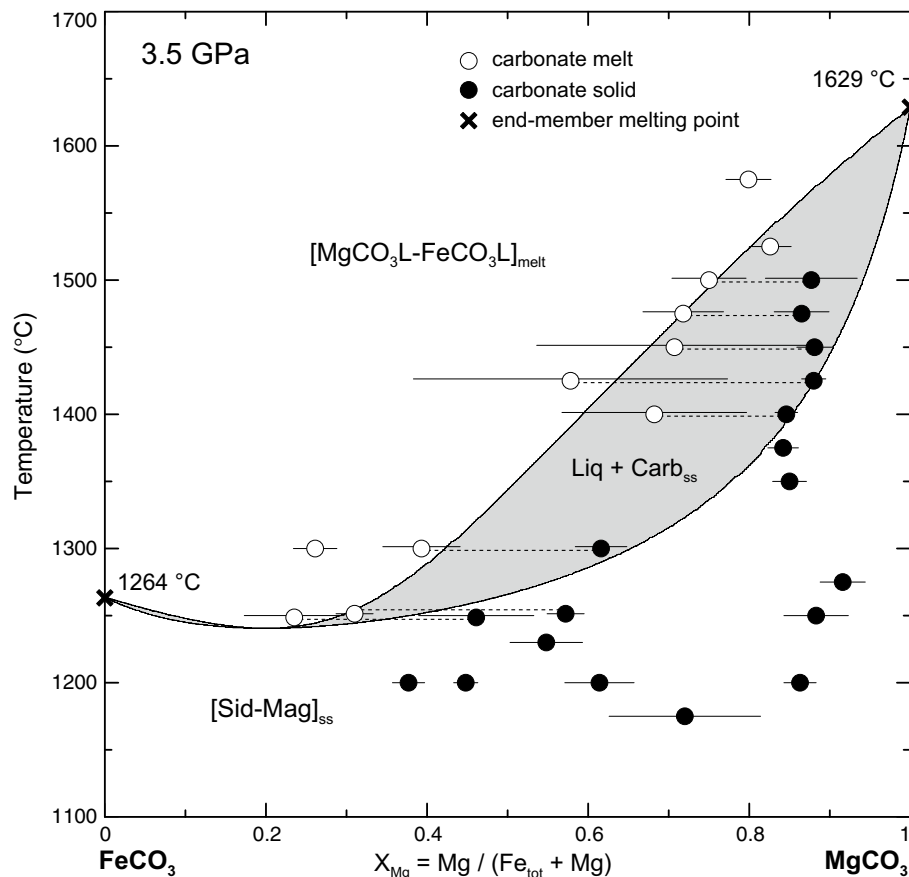


**Fig. 5** Isobaric  $T$ - $X$  diagram in the simple FeCO<sub>3</sub>–MgCO<sub>3</sub> binary at 3.5 GPa, depicting experimental data of stable carbonate solid and liquid pairs with the calculated melting loop employed by Perple\_X 6.6.9 (Connolly 2009). The pure siderite melting temperature is calculated from Kang et al. (2015); note that this melting temperature is metastable. The pure magnesite melting curve is after Irving and Wyllie (1975) and calculated for the pure magnesite melting curve. Standard thermodynamic properties for the end members siderite and FeCO<sub>3</sub>L are adopted from Kang et al. (2015). Thermodynamic data for magnesite and MgCO<sub>3</sub>L are from Merlini et al. (2016)

and this study. We used our melt solution model termed LIQ(NK) combined with the solid solution model for ternary Ca–Mg–Fe carbonates termed dis(EF) from Franzolin et al. (2011). *Dashed lines* represent *tie lines* between coexisting *solid* and *liquid* pairs. *Thin solid lines* display *error bars* in terms of standard deviation. The *symbols* and *error bars* of experiments at 1250 °C are not superimposed for clarity. Note that the Fe-rich side at  $X_{\text{Mg}} < 0.25$  is metastable with respect to magnetite + CO<sub>2</sub> + graphite. The position of the minimum is calculated from the fit of the loop to the experimental data (see text). For abbreviations, see Fig. 1

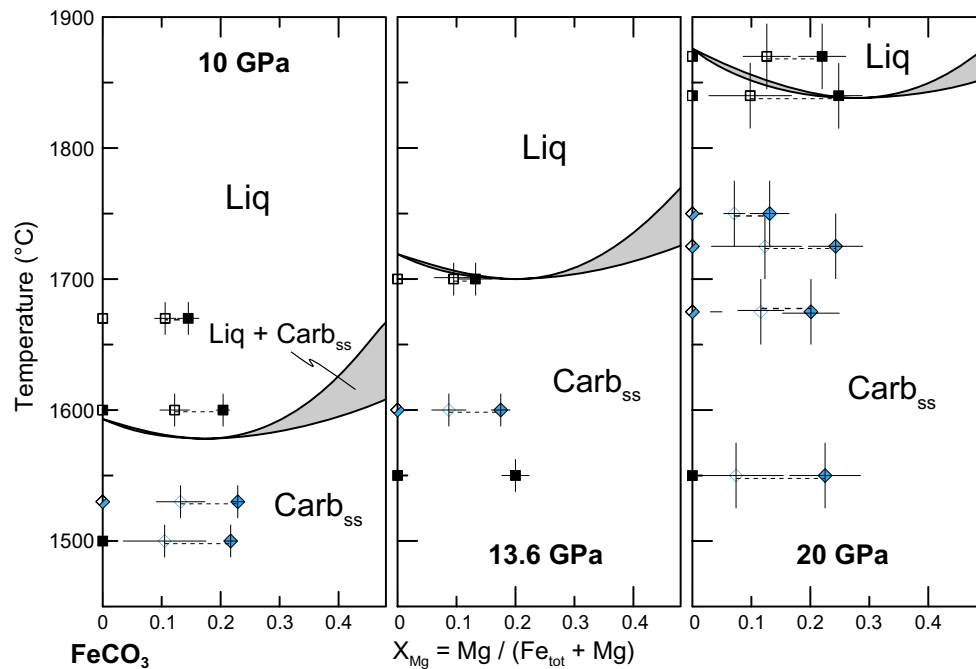


**Fig. 6** Isobaric  $T$ - $X$  sections of the Fe-rich side of the  $\text{FeCO}_3$ – $\text{MgCO}_3$  join at 10, 13.6 and 20 GPa. Experimental compositions of coexisting carbonate solid (filled symbols) and liquid (open symbols) pairs are from this study, and pure siderite experiments are from Kang et al. (2015). Half-filled symbols illustrate partial melting. Blue diamonds indicate experiments with <15 % melt, interpreted as melting in the presence of minor  $\text{H}_2\text{O}$  unavoidable in this kind of starting material. The melting loops including a minimum were calculated

employing *Perple\_X* 6.6.9 (Connolly 2009). Note that the liquid solution model is entirely based on data at 3.5 GPa. The small deviation between the calculated loop and the experimental data at high pressure does not warrant an unideal pressure term in the liquid solution model. The thermodynamic data of all end members are the same as in Fig. 5. Horizontal solid lines are error bars in terms of standard deviation. For abbreviations, see Fig. 1

### The Fe-rich side of the $\text{MgCO}_3$ – $\text{FeCO}_3$ join at 10–20 GPa

Additional melting experiments were performed with the starting compositions  $\text{Mg}_{0.1}\text{Fe}_{0.9}\text{CO}_3$  and  $\text{Mg}_{0.15}\text{Fe}_{0.85}\text{CO}_3$ , to define the Fe-rich side of the siderite–magnesite join at 10, 13.6 and 20 GPa. Textural features of experimental charges and compositions of run products are summarized in Figs. 3 and 6, and experimental data of the pure siderite component are from Kang et al. (2015).

The experimental charges from 10 to 20 GPa are mostly partially molten at temperatures from 1500 to 1890 °C; at 1550 °C, one experiment (SM-05) contains only polygonal carbonate crystals, indicating subsolidus conditions. Similar to the experiments at 3.5 GPa, Mg-bearing siderite melt forms a dendritic texture composed of carbonate quench commonly accompanied with small Fe-rich oxide quench phases (Fig. 3d). In some experiments, melt is a more homogenous carbonate quench showing only minor or no oxide quench (Fig. 3b, c).

The near-solidus experiments are characterized by wide melting intervals spanning 170 °C at 10 GPa, 100 °C at 13.6 GPa and 320 °C at 20 GPa, but over most of these intervals, melt proportions are small and do not exceed

5–15 vol% (Fig. 3b). We explain the appearance of a small melt fraction, increasing little with temperature over a large temperature interval by either absorbed water in the starting material or  $\text{H}_2\text{O}$  resulting from hydrogen diffusion through the capsule wall during the experiment. We hence interpret the solidus of the dry system to occur when large amounts (>30 %) of melt appear in particular as the Fe-rich bulk compositions melt almost congruently. In comparison with the experiments at 3.5 GPa, charges do not contain equilibrium Fe spinel ( $\text{Mt}_{\text{ss}}$ ) or magnesiowustite ( $\text{Mwu}_{\text{ss}}$ ), but only a quench of Fe oxides (magnetite) interstitial to the dendritic quench of carbonates. At all pressure conditions, the compositions of the carbonates and coexisting melt phases are located towards the Fe-rich side (Fig. 6). One experiment (SM-04, 1670 °C, 10 GPa) appears to be inconsistent with all other experiments, and the reason for this remains unclear.

### Thermodynamics of carbonate melts in the system $\text{FeCO}_3$ – $\text{MgCO}_3$

To derive a simple thermodynamic model for carbonate melts from our experiments, we assume that the melt can

**Table 2** Standard molar thermodynamic properties of siderite, magnesite, FeCO<sub>3</sub>L and MgCO<sub>3</sub>L at 298.15 K and 1 bar

Phase	$G_0$ (J)	$H_0$ (J)	$S_0$ (J/K)	$V_0$ (J/bar)	$C_p$ (J/K)	$\alpha_0$ (1/K)	$K_0$ (GPa)	$K'$
Siderite	-790037.4	-762220.0	93.3	2.94	83.07	6.44E-05	123.0	4
FeCO <sub>3</sub> L	-766107.6	-737665.8	95.4	3.18	125.4	6.45E-05	80.23	4
Magnesite	-1130439	-1110910	65.5	2.79	76.11	7.04E-05	108.0	5
MgCO <sub>3</sub> L	-1099104	-1079410	66.1	3.16	124.9	7.04E-05	44.41	5
Fitted coefficients of $C_p$ referred to the polynomial Eq. (10)					Fitted interaction parameter (J/mol)			
	$a$	$b$	$c$	$d$		$w^H$	$w^S$	$w^V$
Siderite	178.8	-3.09E-04	625431	-1773	$W_{\text{sidmag}}$	-7600	0	0
FeCO <sub>3</sub> L	128.5	4.54E-03	246349	-123.7	$W_{\text{magsid}}$	-7600	0	0
Magnesite	185.4	-2.83E-03	24501.6	-1877				
MgCO <sub>3</sub> L	126.4	3.10E-03	72655.2	-54.79				

$G_0$  Gibbs free energy;  $H_0$  enthalpy;  $S_0$  entropy;  $V_0$  volume;  $C_p$  heat capacity;  $\alpha_0$  thermal expansivity;  $K_0$  bulk modulus;  $K'$  pressure derivative of the bulk modulus. Interaction parameters  $W_{\text{sidmag}} = W_{\text{magsid}}$  due to regular solution model

be described as a binary mixture between magnesite and siderite end member compositions, i.e. we neglect the Fe<sup>3+</sup> component and dissolved CO<sub>2</sub> in the melt. We adopt the van Laar model (Holland and Powell 2003) of Franzolin et al. (2011) for fully disordered solid carbonate, which gives the partial molar Gibbs energy of magnesite and siderite as

$$g_i = g_i^0 + R * T * \ln(X_i) + R * T * \ln(\gamma_i) \tag{3}$$

where  $g_i^0$  is the molar Gibbs energy of the pure end member,  $X_i$  its mol fraction in the solution, and the activity coefficient

$$\ln(\gamma_i) = \frac{2 * \alpha_i * (X_j * \alpha_j)^2}{(\alpha_i + \alpha_j) * (\alpha_i * X_i + \alpha_j * X_j)^2} * W_{\text{sol}} \tag{4}$$

with  $\alpha_{\text{mag}} = 1$  J/mol,  $\alpha_{\text{sid}} = 0.01$  J/mol + 0.000666 J/mol \*  $T$ , and  $W_{\text{sol}} = 10000$  J/mol. For the liquid, we assume a regular solution model, such that

$$R * T * \ln(\gamma_i) = (1 - X_i)^2 * W_{\text{liq}} \tag{5}$$

where  $W_{\text{liq}}$  is an interaction parameter to be determined by analysis of the experimental results (Supplementary material). More complex, both subregular and asymmetric formulations for the liquid resulted in models that predicted implausible phase relations. The unknown interaction parameter  $W_{\text{liq}}$  was calculated as the average of the values obtained by solving

$$g_{\text{mag}} = g_{\text{magL}}$$

$$g_{\text{sid}} = g_{\text{sidL}}$$

at the experimentally determined solidus conditions at 3.5 GPa and results to -7600 J/mol. For these calculations, the thermodynamic properties of the end members siderite (Table 2) and siderite melt (FeCO<sub>3</sub>L) are taken from Kang et al. (2015). The caloric properties  $G_0$  and  $S_0$  of magnesite

were adopted from (Holland and Powell 2011), whereas the volumetric data ( $V_0$ ,  $\alpha_0$ ,  $K_0$  and  $K'$ ) are from Merlini et al. (2016). Note that the volume data of Merlini et al. (2016) are consistent with those on siderite and magnesite by Litasov et al. (2008, 2013). The end member data for magnesite liquid (MgCO<sub>3</sub>L) were derived from the congruent melting curve of magnesite. At pressures below 4 GPa, melting of magnesite is observed at ~1585 °C, 3 GPa, and at 1610 °C, 3.6 GPa (Irving and Wyllie 1975). At higher pressures, the melting temperature of MgCO<sub>3</sub> is located at ~1910 °C, 8 GPa, and 2090 °C, 15 GPa (Katsura and Ito 1990). Based on these four experimental brackets, we adopt the following melting curve for pure magnesite

$$T_m(\text{°C}) = 1292.85 + 103.82 * P - 3.38 * P^2 \text{ (P in GPa)}.$$

It is assumed that the temperature dependence of the thermal expansion ( $\alpha_T$ ) and bulk modulus ( $K_T$ ) of all end members are adequately represented by the empirical relations

$$\alpha_T = \alpha_0 * \left(1 - \frac{10}{\sqrt{T}}\right) \tag{6}$$

$$K_T = K_0 \left(1 - 1.5 * 10^{-4} * (T - 298.15)\right) \tag{7}$$

given by Holland and Powell (1998) and volumes are computed from the Murnaghan equation of state

$$V(T, P) = V(T, P_r) * \left[1 - K' * \frac{P}{\{K' * P + K(T, P_r)\}}\right]^{\frac{1}{K'}} \tag{8}$$

The heat capacity of magnesite is adjusted at high temperatures (>2000 K) such that  $C_p$  converges to the Dulong–Petit limit

$$C_P = 3 * R * n + \alpha_T^2 * V_T * K_T * T \quad (9)$$

where  $R$  is the gas constant and  $n$  the number of atoms in the substance of interest. The  $C_P$  of magnesite at low temperatures (<800 K) was computed from Holland and Powell (2011). The total heat capacity range  $C_P(T)$  is then fitted adopting the following polynomial (Holland and Powell 1998)

$$C_P = a + b * T + \frac{c}{T^2} + \frac{d}{\sqrt{T}} \quad (10)$$

The equilibrium condition  $G^{\text{MgCO}_3} = G^{\text{MgCO}_3\text{L}}$  on the melting curve was then used to solve for  $H_0$ ,  $S_0$ ,  $V_0$ ,  $\alpha_0$ , and  $K_0$  of  $\text{MgCO}_3\text{L}$ . The pressure derivative of the bulk modulus  $K'$  for the melt is set to the same value as for the solid, i.e.  $K'(\text{melt}) = K'(\text{solid}) = 5$ . The thermodynamic data of all end members are presented in Table 2.

## Discussion

### The siderite–magnesite melting loop and pure siderite melting

The experimental data and the calculated melting loop in the  $\text{FeCO}_3$ – $\text{MgCO}_3$  system at 3.5 GPa are illustrated in Fig. 5. At 3.5 GPa, only considering the binary siderite–magnesite solid and liquid solutions, our model predicts an asymmetric melting loop (grey field) with both the solid and melt side having a negative deviation from ideal behaviour and a thermal minimum at  $X_{\text{Mg}}$  of 0.2 and ~1240 °C. The exact location and temperature of this minimum is a result of the thermodynamic analysis of the binary. Experiments at 1250 °C provide melt and a melting loop that is still 0.2  $X_{\text{Mg}}$  units wide. Thermodynamic analysis of the pure siderite melting curve from 6 to 20 GPa (Kang et al. 2015) permits calculating the metastable<sup>1</sup> melting curve of siderite to 1264 °C at 3.5 GPa. This result is slightly above the temperature condition where melt in the binary has been observed, suggesting a minimum. At 3.5 GPa, this minimum may lie within the uncertainties of the experiments and thermodynamic calculations; nevertheless, at 10 GPa experiments have been run with two directly adjacent capsules: one with pure siderite (pS-02, Kang et al. 2015) and one with a bulk  $X_{\text{Mg}} = 0.15$  (SM-02). In this single experiment, with both capsules arranged symmetrically at the hot spot, the pure siderite capsule remained unmolten, while the capsule with a bulk  $X_{\text{Mg}}$  of 0.15 showed 10–15 % melt, a clear indication of a minimum.

A non-ideal melting loop contrasts the diagram as drawn by Shatskiy et al. (2015a) who show an ideal melting loop,

based on a few experiments at relatively Fe-rich bulk compositions ( $X_{\text{Mg}} = 0.07$ – $0.35$ ) at 1600–1700 °C at 6 GPa. In comparison with our work, Shatskiy et al. (2015a) used natural siderite containing 6 mol%  $\text{MnCO}_3$  and 7 mol%  $\text{MgCO}_3$ , which may account for some difference in melting temperature. However, Shatskiy et al. (2015a) propose stable melting of siderite at 6 GPa at a temperature slightly below 1600 °C and observe complete melting of their  $\text{Fe}_{0.87}\text{Mn}_{0.06}\text{Mg}_{0.07}\text{CO}_3$  composition at 1700 °C. This is in wild contrast to the experimental data of Tao et al. (2013) and Kang et al. (2015), which show siderite to be stable to 1400 °C but completely decomposed to magnetite + graphite +  $\text{CO}_2$  at 1450 °C, 6 GPa. Note that above 1450 °C magnetite + graphite +  $\text{CO}_2$  form a melt rich in carbonate components. The data of Tao et al. (2013) and Kang et al. (2015) also indicate that direct melting of siderite only occurs above 6 GPa (6.8 GPa in Kang et al. 2015). The metastable pure siderite melting temperature at 6 GPa, as extrapolated from higher pressures, is 1410 °C (Kang et al. 2015). This discrepancy was discussed by Shatskiy et al. (2015a) aiming at experimental artefacts such as Fe loss to the capsule but ignoring the auto-redox decomposition of siderite. It remains unexplained why Tao et al. (2013) and Kang et al. (2015) observe this redox decomposition, while Shatskiy et al. (2015a) do not. Further, if the melting temperature of pure siderite at 6 GPa would be almost 1600 °C instead of 1410 °C, as suggested by Shatskiy et al. (2015a), then at 3.5 GPa the pure siderite melting temperature would have to be considerably higher and the un-ideality and minimum of the system even more pronounced.

At higher pressures of 10–20 GPa (Fig. 6), our experiments only constrain the behaviour of Fe-rich bulk compositions. Our melt model, which does not contain a pressure dependent non-ideal term, indicates a flat minimum topology with melting temperatures from 1580 to 1840 °C, at  $X_{\text{Mg}}$  increasing from 0.2 to 0.28 with pressure. The calculated melting loop (based solely on thermodynamic analysis of the experiments at 3.5 GPa) is in sufficient agreement with the large-scale melting (30–100 %) observed in the experiments at 10–20 GPa and the small melt fractions observed at lower temperatures being interpreted as hydrous melting caused by moisture contamination of the starting material or H-gain through capsule wall diffusion (Fig. 6, diamonds).

### The pseudo-binary nature of $\text{FeCO}_3$ – $\text{MgCO}_3$

Experiments in the  $\text{Fe}$ – $\text{Mg}$ – $\text{C}$ – $\text{O}_2$  system at 3.5 GPa show that siderite decomposition through the auto-redox dissociation reaction (1) or decarbonation of the siderite–magnesite solid solution ( $\text{Sid-Mag}_{\text{ss}}$ ) according to reaction (2) interfere with the carbonate melting reaction in the  $\text{MgO}$ – $\text{FeO}$ – $\text{CO}_2$  system. For that reason, the simple binary  $\text{FeCO}_3$ – $\text{MgCO}_3$

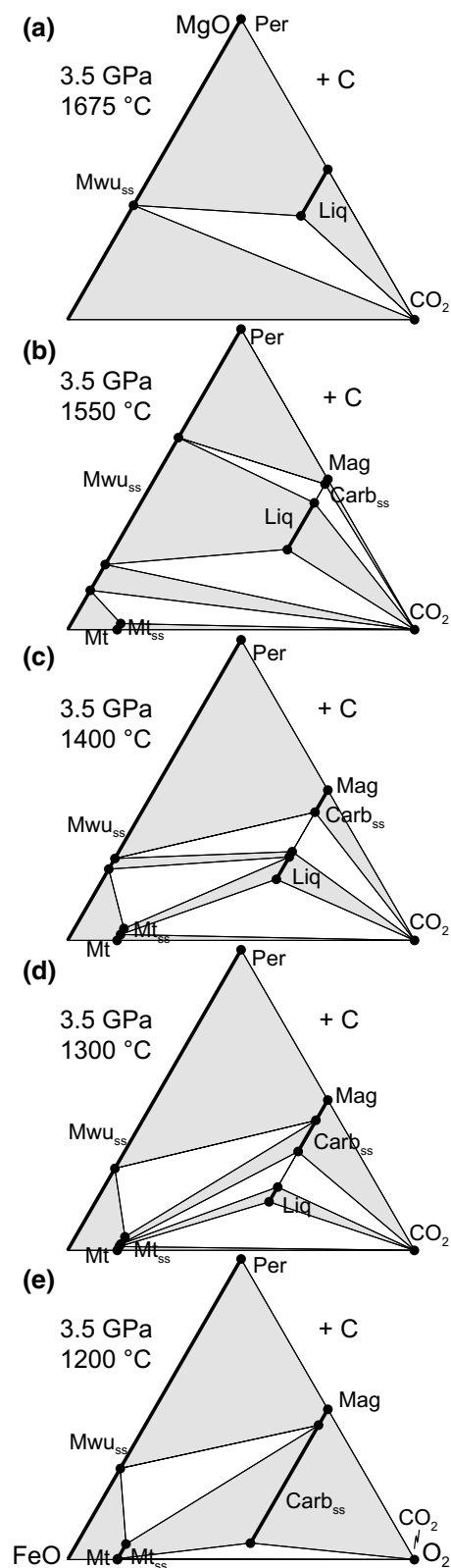
<sup>1</sup> with respect to magnetite + graphite +  $\text{CO}_2$ .

**Fig. 7** Calculated chemographic diagrams in the FeO–MgO–O<sub>2</sub> ternary saturated in graphite, showing stable phase assemblages in isothermal sections from 1200 to 1675 °C employing Perple\_X 6.6.9 (Connolly 2009). For these calculations, we included the ideal solid solution models for magnetite–magnesioferrite (MF) and for periclase–wüstite (P) from Perple\_X in addition to the carbonate models. Initial melting appears between 1200 and 1300 °C, see text. *White triangles* suggest three-phase fields where the phases at their corner points are stable with each other. *Grey fields* represent two-phase fields between opposing mineral assemblages. Solid solutions are indicated by *bold lines*. For abbreviations, see Fig. 1

has in reality the system components MgCO<sub>3</sub>–FeCO<sub>3</sub>–CO<sub>2</sub>–Fe<sub>2</sub>O<sub>3</sub> and is hence a pseudo-binary. However, as long as the carbonate solid and melt are equilibrated, additional phases do not influence this melting equilibrium and its thermodynamic analysis. The decomposition of the siderite component hampers the determination of the melting loop:

1. In the experiments, the formation of Fe-rich oxides through reaction (1) or (2) shifts the bulk carbonate composition away from the siderite side towards MgCO<sub>3</sub> and experiments targeted at the melting loop often result in solid carbonate or melt coexisting with oxides but not in the desired coexisting solid and liquid carbonate. Obviously, when abundant low  $X_{\text{Mg}}$  iron oxides form (Table 1), the carbonate phases alone do not mass balance the bulk composition anymore.
2. Secondly, further problems arise from the reaction products of reactions (1) and (2): both reactions produce CO<sub>2</sub>; this CO<sub>2</sub> was not observed as gas bubbles and is likely to be dissolved in the carbonate melt.
3. Moreover, carbonate liquids do not exclusively quench to carbonates, but into a mixture of carbonate and ferric iron containing oxides clearly visible in BSE images (Fig. 2b, c, d, f) and sometimes identifiable as magnetite by Raman spectroscopy. These textures are consistent with the results of Shatskiy et al. (2015a, b; Figs. 2e, f, h and 1j, respectively), who observe a quench phase from the liquid that is much brighter in BSE images than siderite.

To provide a first-order assessment of the effect of non-stoichiometric melting, carbonate phase equilibria were calculated in the system MgO–FeO–O–C including magnetite–magnesioferrite and magnesio-wüstite solid solutions in addition to the carbonate models (Figs. 7, 8, 9). Graphite-saturated phase relations for this system are presented in 5 isothermal triangular chemographic sections calculated for 1200 to 1675 °C at 3.5 GPa (Fig. 7). The graphite-only saturation condition allows for three coexisting Fe–Mg phases; as observed in many experiments, in this case CO<sub>2</sub> saturation cannot occur and the carbonate melt would be the only liquid phase.



The same MgO–FeO join is projected from C and CO<sub>2</sub> such that  $f_{\text{O}_2}$  is constrained to the C–CO–CO<sub>2</sub> (CCO) buffer into a  $T$ - $X$  diagram (Fig. 8). These phase equilibria

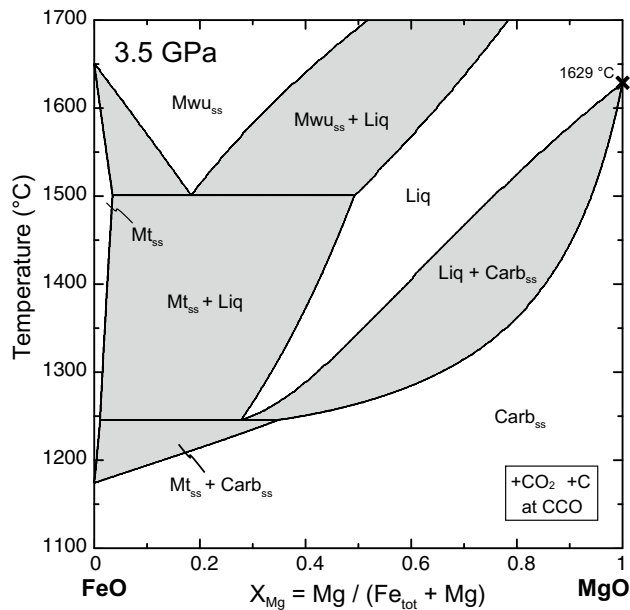


**Fig. 8** Calculated isobaric  $T$ - $X$  diagram along the FeO–MgO join projected through CCO, i.e. saturated in  $\text{CO}_2$  fluid and graphite at 3.5 GPa employing *Perple\_X* 6.6.9 (Connolly 2009). The solution models used in this computation are the same as in Fig. 7.  $\text{CO}_2$  is chosen as the independent saturated fluid component and  $\text{O}_2$  as the saturated or buffered component. The fluid EoS is  $X(\text{O})$  GCOH-fluid hybrid EoS from Connolly and Cesare (1993). Carbonates are unstable near the siderite side where magnetite–magnesiowustite solid solution forms. Note that the melting loop at the Fe-rich side is metastable, for comparison see Fig. 5. For details of the Fe-oxidation, see text. Thermodynamic properties of wustite, periclase, magnetite and magnesiowustite are from Holland and Powell (2011). The thermodynamic data set of Fe–Mg carbonates and their melts are the same as described in Fig. 5. For abbreviations, see Fig. 1

calculations confirm the experimental observations (Fig. 4) that siderite-rich carbonate phases become unstable at 3.5 GPa and will always transform into ferric components forming  $\text{Mt}_{\text{ss}}$  below  $\sim 1500$  °C at the Fe side of this pseudo-binary. Above  $\sim 1500$  °C, the computation predicts stability fields for magnesiowustite coexisting with the carbonate liquid field towards the Mg side along the FeO–MgO join projected through  $\text{O}_2$  and C, as it is depicted in the chemographic triangles in Fig. 7. In the experiments, we used inner graphite capsules, but fluid vapour bubbles of  $\text{CO}_2$  were not observed at 3.5 GPa; hence, the experimental  $f_{\text{O}_2}$  may well be below CCO.

A calculation at 1400 °C, 3.5 GPa in  $\log(f_{\text{O}_2})$  versus  $X_{\text{Mg}}$  space, expanded around CCO, suggests that small variations in  $f_{\text{O}_2}$  below CCO would have a large effect on the magnesiowustite composition and on liquid compositions (Fig. 9), but would cause little or marginal differences in the  $\text{Mt}_{\text{ss}}$  stability. The computed phase diagram also shows that below an  $f_{\text{O}_2}$  of CCO–0.4 the stability range of Fe–Mg carbonates decreases distinctively towards the Mg side along the FeO–MgO join. The carbonate melt compositions

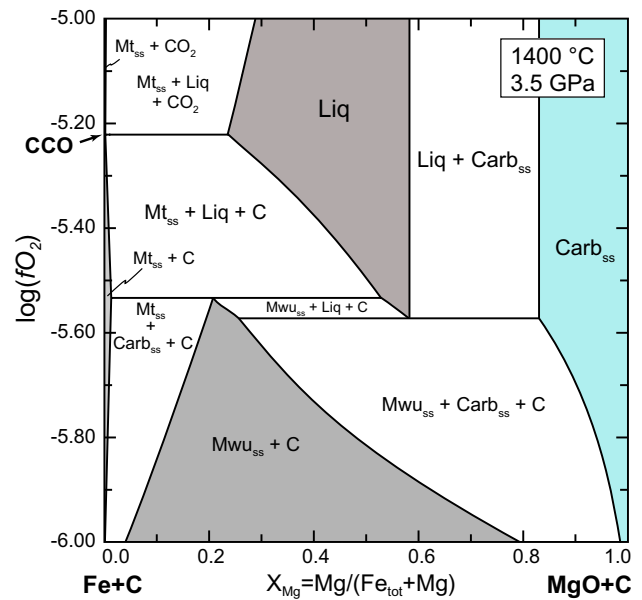


**Fig. 9** Calculated phase relations in  $\log(f_{\text{O}_2})$  versus  $X_{\text{Mg}} = \text{Mg}/(\text{Fe}_{\text{tot}} + \text{Mg})$  expanded around the CCO buffer at 1400 °C, 3.5 GPa portraying that small variations in  $f_{\text{O}_2}$  have large effects on magnesiowustite and on carbonate liquid compositions. As the experiments are most probably below CCO, the phase equilibria computation is in good agreement with the experimental observations of  $\text{Mwu}_{\text{ss}}$  compositions deviating to higher  $X_{\text{Mg}}$  due to the change of  $f_{\text{O}_2}$ . This effect is prominently important, since carbonates become unstable to very low  $f_{\text{O}_2}$  towards the Mg side of this pseudo-binary. Note that the stability boundaries of the carbonate liquid and solid field would slightly extended at higher  $f_{\text{O}_2}$  due to the ferric iron component in the melt. The solution models used are the same as in Figs. 7 and 8

are not located on the same binary of the solid carbonates, analogous to the diopside–anorthite–albite system, where liquids are expected to be on a cotectic; see Fig. 10.25 in Philpotts (1990). Our two-component thermodynamic melt model includes hence a deviation of the melt composition from the simple binary, a situation not much different from many solid solutions, where pure ferrous end members do not exist but always contain some ferric iron (e.g. biotite, staurolite, sapphirine, talc).

## Concluding remarks

In this study, we present experiments on the  $\text{FeCO}_3$ – $\text{MgCO}_3$  join at 3.5–20 GPa, which allow depicting the melting loop in  $T$ - $X$  diagrams. The melting loop is asymmetrical and has a thermal minimum at Fe-rich bulk compositions. A regular solution model is adequate to represent these phase relations over the pressure–temperature range of our observations. Interpretation of the system at Fe-rich compositions is complicated by problems of  $\text{Fe}^{2+}$  oxidation and excess  $\text{CO}_2$  dissolved in the melt. For the melting of

basaltic and peridotitic bulk compositions, a liquid Fe carbonate end member is needed to calculate phase relations, although the dominant carbonate melt components are the Mg and Ca ones. For carbonated pelites, partial carbonate melts may reach down to  $X_{\text{Mg}} = 0.24$  (Grassi and Schmidt 2011); at the extreme, banded iron formations may produce almost pure siderite melts.

**Acknowledgments** Thanks to L. Ramalingam for conducting some of the siderite–magnesite experiments at 3.5 GPa. We are thankful to C. Liebske for discussion and technical support in the laboratory and to T. Good and B. Zürcher for mechanical support. We also thank X. Zhong and D. Miron for discussions about thermodynamic solution models. This study was made possible through grant SNF-200020-130100/1 and 200020-140541/1.

## References

- Beukes NJ, Gutzmer J (2008) Origin and paleoenvironmental significance of major iron formations at the archean-paleoproterozoic boundary. *Band Iron Form Relat High Grade Iron Ore* 15:5–47
- Biehlmann C, Gillet P, Guyot F, Peyronneau J, Reynard B (1993) Experimental-evidence for carbonate stability in the earth's lower mantle. *Earth Planet Sci Lett* 118:31–41
- Boulard E, Menguy N, Auzende AL, Benzerara K, Bureau H, Antonangeli D, Corgne A, Morard G, Siebert J, Perrillat JP, Guyot F, Fiquet G (2012) Experimental investigation of the stability of Fe-rich carbonates in the lower mantle. *J Geophys Res* 117:B02208
- Breary AJ, Rubie DC (1990) Effects of H<sub>2</sub>O on the disequilibrium breakdown of muscovite + quartz. *J Petrol* 31:925–956
- Brey GP, Bulatov VK, Girmis AV, Lahaye Y (2008) Experimental melting of carbonated peridotite at 6–10 GPa. *J Petrol* 49:797–821
- Brey GP, Bulatov VK, Girmis AV (2009) Influence of water and fluorine on melting of carbonated peridotite at 6 and 10 GPa. *Lithos* 112:249–259
- Buckley HA, Woolley AR (1990) Carbonates of the magnesite siderite series from 4 carbonatite complexes. *Miner Mag* 54:413–418
- Connolly JAD (2009) The geodynamic equation of state: what and how. *Geochem Geophys Geosyst*. doi:10.1029/2009GC002540
- Connolly JAD, Cesare B (1993) C–O–H–S fluid composition and oxygen fugacity in graphitic metapelites. *J Metamorph Geol* 11:379–388
- Dasgupta R, Hirschmann MM (2006) Melting in the earth's deep upper mantle caused by carbon dioxide. *Nature* 440:659–662
- Dasgupta R, Hirschmann MM (2010) The deep carbon cycle and melting in Earth's interior. *Earth Planet Sci Lett* 298:1–13
- Dasgupta R, Hirschmann MM, Withers AC (2004) Deep global cycling of carbon constrained by the solidus of anhydrous, carbonated eclogite under upper mantle conditions. *Earth Planet Sci Lett* 227:73–85
- Dasgupta R, Hirschmann MM, Dellas N (2005) The effect of bulk composition on the solidus of carbonated eclogite from partial melting experiments at 3 GPa. *Contrib Miner Petrol* 149:288–305
- Davidson PM (1994) Ternary iron, magnesium, calcium carbonates—a thermodynamic model for dolomite as an ordered derivative of calcite-structure solutions. *Am Miner* 79:332–339
- Dobson DP, Brodholt JP (2005) Subducted banded iron formations as a source of ultralow-velocity zones at the core-mantle boundary. *Nature* 434:371–374
- Eiler JM, Valley JW, Graham CM, Fournelle J (2002) Two populations of carbonate in ALH84001: geochemical evidence for discrimination and genesis. *Geochim Cosmochim Acta* 66:1285–1303
- Falloon TJ, Green DH (1989) The solidus of carbonated, fertile peridotite. *Earth Planet Sci Lett* 94:364–370
- Fiquet G, Guyot F, Kunz M, Matas J, Andrault D, Hanfland M (2002) Structural refinements of magnesite at very high pressure. *Am Miner* 87:1261–1265
- Franzolin E, Schmidt MW, Poli S (2011) Ternary Ca–Fe–Mg carbonates: subsolidus phase relations at 3.5 GPa and a thermodynamic solid solution model including order/disorder. *Contrib Miner Petrol* 161:213–227
- French BM (1971) Stability relations of siderite (FeCO<sub>3</sub>) in system Fe–C–O. *Am J Sci* 271:37–78
- Ghosh S, Ohtani E, Litasov KD, Terasaki H (2009) Solidus of carbonated peridotite from 10 to 20 GPa and origin of magnesiocarbonatite melt in the Earth's deep mantle. *Chem Geol* 262:17–28
- Goldsmith JR, Graf DL, Witters J, Northrop DA (1962) Studies in the system CaCO<sub>3</sub>–MgCO<sub>3</sub>–FeCO<sub>3</sub>. 1. Phase relations. 2. A method for major-element spectrochemical analysis. 3. Compositions of some ferroan dolomites. *J Geol* 70:659–688
- Grassi D, Schmidt MW (2011) Melting of carbonated pelites at 8–13 GPa: generating K-rich carbonatites for mantle metasomatism. *Contrib Miner Petrol* 162:169–191
- Holland TJB, Powell R (1998) An internally consistent thermodynamic data set for phases of petrological interest. *J Metamorph Geol* 16:309–343
- Holland TJB, Powell R (2003) Activity-composition relations for phases in petrological calculations: an asymmetric multicomponent formulation. *Contrib Miner Petrol* 145:492–501
- Holland TJB, Powell R (2011) An improved and extended internally consistent thermodynamic dataset for phases of petrological interest, involving a new equation of state for solids. *J Metamorph Geol* 29:333–383
- Irving AJ, Wyllie PJ (1975) Subsolidus and melting relationships for calcite, magnesite and join CaCO<sub>3</sub>–MgCO<sub>3</sub> to 36 Kb. *Geochim Cosmochim Acta* 39:35–53
- Isshiki M, Irifune T, Hirose K, Ono S, Ohishi Y, Watanuki T, Nishibori E, Takata M, Sakata M (2004) Stability of magnesite and its high-pressure form in the lowermost mantle. *Nature* 427:60–63
- Kang N, Schmidt MW, Poli S, Franzolin E, Connolly JAD (2015) Melting of siderite to 20 GPa and thermodynamic properties of FeCO<sub>3</sub>-melt. *Chem Geol* 400:34–43
- Katsura T, Ito E (1990) Melting and subsolidus phase-relations in the MgSiO<sub>3</sub>–MgCO<sub>3</sub> system at high-pressures—implications to evolution of the earth's atmosphere. *Earth Planet Sci Lett* 99:110–117
- Keppeler H, Wiedenbeck M, Shcheka SS (2003) Carbon solubility in olivine and the mode of carbon storage in the Earth's mantle. *Nature* 424:414–416
- Kerrick DM, Connolly JAD (2001a) Metamorphic devolatilization of subducted marine sediments and the transport of volatiles into the Earth's mantle. *Nature* 411:293–296
- Kerrick DM, Connolly JAD (2001b) Metamorphic devolatilization of subducted oceanic metabasalts: implications for seismicity, arc magmatism and volatile recycling. *Earth Planet Sci Lett* 189:19–29
- Kholodov VN, Butuzova GY (2008) Siderite formation and evolution of sedimentary iron ore deposition in the Earth's history. *Geol Ore Depos* 50:299–319
- Klein C (2005) Some precambrian banded iron-formations (BIFs) from around the world: their age, geologic setting, mineralogy, metamorphism, geochemistry, and origin. *Am Miner* 90:1473–1499
- Klein-BenDavid O, Logvinova AM, Schrauder M, Spetius ZV, Weiss Y, Hauri EH, Kaminsky FV, Sobolev NV, Navon O (2009) High-Mg carbonatitic microinclusions in some Yakutian diamonds—a new type of diamond-forming fluid. *Lithos* 112:648–659

- Koziol AM (2004) Experimental determination of siderite stability and application to martian meteorite ALH84001. *Am Miner* 89:294–300
- Litasov KD, Fei YW, Ohtani E, Kuribayashi T, Funakoshi K (2008) Thermal equation of state of magnesite to 32 GPa and 2073 K. *Phys Earth Planet Int* 168:191–203
- Litasov KD, Shatskiy A, Gavryushkin PN, Sharygin IS, Dorogokupets PI, Dymshits AM, Ohtani E, Higo Y, Funakoshi K (2013) P–V–T equation of state of siderite to 33 GPa and 1673 K. *Phys Earth Planet Int* 224:83–87
- Mann U, Schmidt MW (2015) Melting of pelitic sediments at subarc depths: 1. Flux versus fluid-absent melting and a parameterization of melt productivity. *Chem Geol* 404:150–167
- Merlini M, Tumiati S, Lotti P, Sapelli F, Fumagalli P, Gatta D, Abdelatif M, Plaisier J, Lausi A, Hanfland M, Crichton W, Chantel J, Guignard J, Pavese A, Poli S (2016) High-temperature and high-pressure behavior of carbonates in the ternary diagram  $\text{CaCO}_3\text{--MgCO}_3\text{--FeCO}_3$ . *Am Miner* 101:1423–1430
- Molina JF, Poli S (2000) Carbonate stability and fluid composition in subducted oceanic crust: an experimental study on  $\text{H}_2\text{O--CO}_2$ -bearing basalts. *Earth Planet Sci Lett* 176:295–310
- Morris RV, Ruff SW, Gellert R, Ming DW, Arvidson RE, Clark BC, Golden DC, Siebach K, Klingelhofer G, Schroder C, Fleischer I, Yen AS, Squyres SW (2010) Identification of carbonate-rich outcrops on mars by the spirit rover. *Science* 329:421–424
- Panero WR, Kabbes JE (2008) Mantle-wide sequestration of carbon in silicates and the structure of magnesite II. *Geophys Res Lett* 35:L14307. doi:10.1029/2008GL034442
- Pask JA (1996) Importance of starting materials on reactions and phase equilibria in the  $\text{Al}_2\text{O}_3\text{--SiO}_2$  system. *J Eur Ceram Soc* 16:101–108
- Philipp RW (1998) Phasenbeziehungen im system  $\text{MgO--H}_2\text{O--CO}_2\text{--NaCl}$ . Dissertation. ETH Zurich
- Philpotts AR (1990) Principles of igneous and metamorphic petrology Anthony R. Philpotts. Prentice Hall, Englewood Cliffs, p 498
- Polat A, Hofmann AW, Rosing MT (2002) Boninite-like volcanic rocks in the 3.7–3.8 Ga Isua greenstone belt, West Greenland: geochemical evidence for intra-oceanic subduction zone processes in the early Earth. *Chem Geol* 184:231–254
- Poli S, Franzolin E, Fumagalli P, Crottini A (2009) The transport of carbon and hydrogen in subducted oceanic crust: an experimental study to 5 GPa. *Earth Planet Sci Lett* 278:350–360
- Putnis A (1992) An introduction to mineral sciences. Cambridge University Press, Cambridge, p 480
- Rosenberg PE (1967) Subsolidus relations in system  $\text{CaCO}_3\text{--MgCO}_3\text{--FeCO}_3$  between 350° and 550 °C. *Am Miner* 52:787–796
- Rubie DC, Brearley AJ (1990) A model for rates of disequilibrium melting during metamorphism. High-temperature metamorphism and crustal anatexis. Volume 2 of the series. The mineralogical society series, pp 57–86
- Shatskiy A, Litasov KD, Ohtani E, Borzdov YM, Khmel'nikov AI, Palyanov YN (2015a) Phase relations in the  $\text{K}_2\text{CO}_3\text{--FeCO}_3$  and  $\text{MgCO}_3\text{--FeCO}_3$  systems at 6 GPa and 900–1700 °C. *Eur J Miner* 27(4):487–499
- Shatskiy A, Rashchenko SV, Ohtani E, Litasov KD, Khlestov MV, Borzdov YM, Kupriyanov IN, Sharygin IS, Palyanov YN (2015b) The system  $\text{Na}_2\text{CO}_3\text{--FeCO}_3$  at 6 GPa and its relation to the system  $\text{Na}_2\text{CO}_3\text{--FeCO}_3\text{--MgCO}_3$ . *Am Miner* 100:130–137
- Shcheka SS, Wiedenbeck M, Frost DJ, Keppler H (2006) Carbon solubility in mantle minerals. *Earth Planet Sci Lett* 245:730–742
- Stachel T, Harris JW, Brey GP, Joswig W (2000) Kankan diamonds (Guinea) II: lower mantle inclusion parageneses. *Contrib Miner Petrol* 140:16–27
- Stewart AJ, van Westrenen W, Schmidt MW, Melekhova E (2006) Effect of gasketing and assembly design: a novel 10/3.5 mm multi-anvil assembly reaching perovskite pressures. *High Press Res* 26:293–299
- Tao RB, Fei YW, Zhang LF (2013) Experimental determination of siderite stability at high pressure. *Am Miner* 98:1565–1572
- Thomsen TB, Schmidt MW (2008) Melting of carbonated pelites at 2.5–5.0 GPa, silicate-carbonatite liquid immiscibility, and potassium-carbon metasomatism of the mantle. *Earth Planet Sci Lett* 267:17–31
- Wallace ME, Green DH (1988) An experimental-determination of primary carbonatite magma composition. *Nature* 335:343–346
- Wang A, Pasteris JD, Meyer HOA, DeleDuboi ML (1996) Magnesite-bearing inclusion assemblage in natural diamond. *Earth Planet Sci Lett* 141:293–306
- Weidner JR (1972) Equilibria in system  $\text{Fe--C--O}$ . 1. Siderite-magnetite-carbon-vapor equilibrium from 500 to 10,000 bars. *Am J Sci* 272:735–751
- Yaxley GM, Brey GP (2004) Phase relations of carbonate-bearing eclogite assemblages from 2.5 to 5.5 GPa: implications for petrogenesis of carbonatites. *Contrib Miner Petrol* 146:606–619
- Yaxley GM, Green DH (1994) Experimental demonstration of refractory carbonate-bearing eclogite and siliceous melt in the subduction regime. *Earth Planet Sci Lett* 128:313–325